Journal of Zhejiang University-SCIENCE A (Applied Physics & Engineering)
ISSN 1673-565X (Print); ISSN 1862-1775 (Online)
www.zju.edu.cn/jzus; www.springerlink.com
E-mail: jzus@zju.edu.cn

Buckling design of large steel silos with various slendernesses*

Qing-shuai CAO, Yang ZHAO†‡
(*Space Structures Research Center, Zhejiang University, Hangzhou 310058, China*)
†E-mail: ceyzhao@zju.edu.cn

Received May 12, 2016; Revision accepted July 4, 2016; Crosschecked Mar. 9, 2017

Abstract: Large steel silos are typical kinds of thin-walled structure which are widely used for storing huge quantities of granular solids in industry and agriculture. In the present analyses, the buckling design of large steel silos subject to Eurocode-specified solid pressure is demonstrated. The finite element model is established using the commercial general purpose computer package ANSYS. Six types of buckling analyses are carried out for the geometrically perfect and imperfect models with and without consideration of material plasticity. The load cases of concentric discharge, discharge patch load, large eccentricity discharge, and large eccentricity filling are considered. The buckling behavior of six example steel silos with capacities of 30 000–60 000 m^3 is investigated. The silos' slenderness ranges from 4.77 to 0.35, comprising very slender, slender, intermediate slender, squat, and retaining silos. The index called the ratio of capacity to steel consumption (RCS) is initially defined in the paper, which provides an effective measure for the economical design of steel silos. It is validated that the RCS index increases rapidly with the decrease of silo slenderness, and the storage efficiency of steel silo improved greatly as the slenderness changes from slender silo to retaining silo. The effects of patch load reveal that the buckling modes in the case of discharge patch load are very different from those of silos under concentric solid pressure, and the effect is unfavorable for buckling resistance of all levels of slenderness of the example silos, but contributes a small decrease to the RCS index (less than 10%). The buckling deformations from both the linear and nonlinear buckling analyses in large eccentric discharge are strongly asymmetrical arising from the circumferential and meridional non-uniform distribution of the solid pressures. The buckling is mainly governed by the non-uniform distribution of the solid pressure other than other influential factors such as the weld imperfection, geometrical and material nonlinearity, compared with the load case of concentric discharge. The RCS index of example silos under large eccentric discharge is reduced substantially, and is approximately half that of silos under concentric discharge. The linear and nonlinear buckling deformations in large eccentric filling are also asymmetrical, deviating from the center to the side where the most friction locates to the highest wall contact. The RCS index of example silos under large eccentric filling is also reduced substantially, and is approximately 70% that of silos under concentric discharge. This reveals that the large eccentricity both in discharging and filling could result in a strong decrease of storage efficiency of steel silos.

Key words: Steel silo; Shell, Slenderness; Buckling; Patch load; Nonlinear; Large eccentricity
http://dx.doi.org/10.1631/jzus.A1600369 **CLC number:** TH161.12

1 Introduction

Silos are usually constructed in a vertically circular form and are used as vessels for storing particulate granular solids filled by gravity at the top. Depending on the geometry and capacity of steel silos, they may be supported in two fundamental manners, discrete support and continuous support. Discrete support is applicable for silos with small diameter constructed using a local bracket or column, giving a limited number of narrow supports around the silo circumference, and continuous support refers to the silo with large diameter (such as silo diameter larger than 15 m) which is supported exactly on the bottom plate with the underpass beneath the flat bottom (BSI, 2002b; 2005; 2006; 2007a; 2007b). Large

‡ Corresponding author
* Project supported by the National Natural Science Foundation of China (No. 51378459)
ORCID: Qing-shuai CAO, http://orcid.org/0000-0002-9405-1858; Yang ZHAO, http://orcid.org/0000-0001-6880-0504

steel silos widely used for storing huge quantities of granular solids in industry and agriculture are usually continuously supported on the ground and consist of a rigid flat bottom, a cylindrical shell with stepped wall thickness, and a conical or dome roof on the top.

At present, steel silo development is at a critical point with a boom in capacity requirement and a number of practical engineering developments in recent years. On the one hand, there is a great need for large steel silos with capacities of over 10000 m^3 given the development of the world economy, and on the other, there is a paucity of studies on the structural behavior, especially buckling, under solid pressures. There is a need for further study through many site measurements and numerical analyses, even though buckling behavior of small capacity steel silos has been reported (Sadowski and Rotter, 2011a; 2011b; 2011c). Ever larger capacity steel silos are now being developed with the aid of automation and mechanization and this provides an improvement in productivity and economic investment. Steel silos with the diameter of 60 m or even more than 100 m are also frequently reported, whose contents may be more than 100000 m^3. A practical ground-supported circular steel silo, which is constructed in Liaoning Province, China with diameter of about 45 m and height of 36 m (capacity 57000 m^3), is shown in Fig. 1.

Fig. 1 A practical ground-supported circular steel silo

The structural design of circular steel silos is well known to be usually controlled by considerations of buckling under axial compressive stress with the buckling deformation as the potential failure mode. The design is complicated, as illustrated by the relevant current European standards (BSI, 2002a; 2002b; 2005). The design rules differ greatly depending on the distribution and magnitude of action, e.g., under loading shown by the design criteria in different standards (ISO, 1995; Standards Australia, 1996; BSI, 2002b; 2005). There are two key issues which require to be examined before the design can be implemented, one is the determination of wall pressures induced by the stored granular solids, and the other is connected with the buckling investigation of a silo which is subject to combined horizontal pressure and vertical friction. With the recent advances of the finite element method (FEM) and the numerical algorithm, it is now reasonably convenient for the researchers to perform numerical analyses of steel cylindrical shells (Li *et al.*, 2005; Zhao *et al.*, 2006) under complex loading patterns and boundary conditions. The buckling behavior of cylindrical steel shells under axial compression has been the most commonly researched aspect (Greiner and Guggenberger, 1998; Kim and Kim, 2002). The review of recent research advances and trends in the area of stability of un-stiffened circular cylindrical shells subject to general non-uniform axial compressive stresses was provided by Song (2002). Design results of the finite element (FE) investigation into the buckling strengths of steel silos subject to code-specified pressures for eccentric discharge were presented by Song and Teng (2003), which indicate that the effect of patch loads from different codes on nonlinear buckling loads is small, and the axisymmetric primary wall loads are shown to control the buckling loads. The structural behaviour of silos supported on discrete eccentric brackets was presented by Gillie and Holst (2003), considering the effects of bracket width, bracket height, and geometric imperfections. It is found that the bracket-supported silos are generally imperfection insensitive, and the strength is strongly but nonlinearly dependent on the bracket width and height. Song (2004) also studied the effects of patch loads on the structural behavior of circular flat-bottomed steel silos, and concludes that patch loads have a great effect on the stress states in the silo according to linear elastic analysis (LA). Geometrical nonlinearity and primary pressures have a beneficial effect. The effects of patch loads on thin-walled steel silos were also evaluated by Gillie and Rotter (2002). The results show that the stresses set up are complex and that they could potentially lead to failure of the silo by either elastic

buckling or plastic collapse. The circumferential width of the applied load and the pressure distribution both strongly affect the form and magnitude of the stresses produced in the silo wall. Most importantly, weld imperfections have been reported to have a detrimental effect on the buckling resistance of silos under axial load. The impact of circumferential weld imperfections was investigated using the FEM by Pircher and Bridge (2001), and it was found that the influence on the buckling behavior depended on the strake height in relation to the linear meridional bending half-wavelength and the depth of the imperfection. The elastic buckling strengths of imperfect cylindrical silos containing granular solids were also examined by Rotter and Zhang (1990), with imperfections in the form of a depression at a circumferential welded joint, and it was suggested that the restrain effect of granular solid may be incorporated into the buckling calculation. Based on the current European standard, the buckling behaviour of small capacity cylindrical steel silos with stepwise wall thickness and aspect ratios varying from very squat to very slender was explored for both perfect and imperfect models under concentric and eccentric discharge by Sadowski and Rotter (2011b), which showed that the aspect ratio plays a deciding role in both the behaviour and design of silos.

Thin-walled circular silos with stepped wall thickness were studied for eccentric discharge pressure by Sadowski and Roster (2011c), which showed that a silo design that was found to be very safe under concentric discharge pressures becomes very unsafe under eccentric discharge. With the assumption of a parallel-sided flow channel, Sadowski and Roster (2011a) explored further the buckling behavior of very slender silos under eccentric discharge. These were examined using geometrically and materially nonlinear analyses. The mechanics of the nonlinear behavior of a cylindrical silo under eccentrically discharge was explored using the analogy of a propped cantilever slice beam to describe the nonlinear behavior of cylindrical shells (Sadowski and Rotter, 2013). The effects of patch loads on thin-walled steel silos were also evaluated by Gillie and Rotter (2002) and Song (2004), and the studies concluded that patch loads have a great effect on the stresses in the silo from the LA (Song, 2004) and that they could potentially lead to failure of the silo by either elastic buckling or plastic collapse (Gillie and Rotter, 2002). Thin-walled steel silos were also found to be generally sensitive to imperfections (Rotter and Zhang, 1990); a detailed parametric study was presented into the behavior of a slender silo under asymmetrical pressures describing the action of an eccentric parallel-sided pipe flow channel of varying cross section, which reveals that geometric nonlinearity is of much greater significance for cylindrical shells under asymmetrical load patterns than under symmetrical patterns, and that eigenmode-affine imperfections, which are deleterious under axisymmetric loading patterns, are instead beneficial to the buckling strength of a silo under eccentric discharge, thus making them unsuitable for use in any design for this load condition (Sadowski and Rotter, 2012). The stability process in a silo is investigated using a static and dynamic FE analysis by taking both the geometric and material nonlinearity into account during eccentric discharge. The differences between the results of static and dynamic analyses were comprehensively discussed (Iwicki *et al*., 2014).

This paper investigates the buckling behavior of large steel silos with capacities of 30 000–60 000 m^3 through numerical analyses, with slenderness ranges from 4.77 to 0.35, which we can characterize as very slender, slender, intermediate slender, squat, and retaining silos. In this study, the details of geometry and capacity of the example silos are first presented in Section 2 together with their design conditions. Then, we describe the analysis for example silos including the geometrically perfect and imperfect FE models and the types of buckling analyses (Section 3). In Section 4, we give the definition of buckling resistance of steel silos. The numerical results for concentric discharge of the example silos with various slendernesses are presented for both the perfect and imperfect models in all proposed buckling analyses in Section 5 and the assessments of the different consequences of different load cases are also made for the buckling resistance and buckling mode. The buckling behaviors of the example silos under large eccentricity discharge and large eccentricity filling are evaluated in Sections 6 and 7, respectively, for both the perfect and imperfect models in all proposed buckling analyses. At the end, some conclusions

expected to benefit the understanding of the buckling behavior of steel silos subject to solid pressures are obtained.

2 Geometry of example silos and solid pressure

Large circular steel silos with capacities of 30 000–60 000 m^3 as used in practice are chosen as illustrative examples in this study, and the geometries of the six silos are listed in Table 1. The examples cover every category of silo slenderness specified in EN 1991-4 (BSI, 2006), the very slender (slenderness h_c/d_c>4.0, where h_c is the height of vertical-walled segment of silo from transition to equivalent surface, and d_c is the dimension of inside of silo cross-section), slender ($2.0\le h_c/d_c\le 4.0$), intermediate slender ($1.0< h_c/d_c<2.0$), squat ($0.4<h_c/d_c\le 1.0$), and retaining ($h_c/d_c\le 0.4$) silos, and also cover a very wide range of silo geometry, the diameter d_c ranging from 20 m to 60 m, and the height h_c ranging from about 21 m to 95 m. The geometries of steel silos which are in service are basically incorporated within this range. A steel silo with diameter of 45 m and height of 36 m (capacity 57 000 m^3) is shown in Fig. 1.

Buckling analyses for exploring the ultimate limit state of silos depend strongly on the following working conditions: the action assessment class (Table 2.1, BSI, 2006), the fabrication tolerance quality class (Table 5.1, BSI, 2007b), and the consequence class (Table 2.1, BSI, 2007b), which take account of the influence of the silo capacity, the supporting patterns, and the eccentricity during filling and discharge, and the weld imperfection of silo wall (Rotter and Teng, 1989), etc., as appropriate. In this study, large steel silos constructed with plain rolled steel sheets are taken as the reference examples whose contents are usually more than 30 000 t in normal service life, as listed in Table 1. The associated requirements of the above design conditions for buckling assessment are specified in Eurocodes. The appropriate design conditions are summarized and listed in Table 2.

Table 2 Design conditions assumed for the numerical analyses

Design condition	Class
Action assessment	AAC3
Fabrication tolerance quality	Class B (high: quality parameter Q=25)
Consequence class	CC3
Wall surface	D1 (slippery)

The distribution patterns and magnitudes of pressures on the silo wall exerted by the stored granular solid have been a crucial problem in the design of silos. In the currently published Eurocode (BSI, 2006), principles for the determination of pressures on the vertical walls of silos are provided so that the wall pressures induced by stored bulk solids during the filling and discharge shall be evaluated according to the slenderness of the silo. The pressures on the vertical wall of silo induced by the stored bulk solids during concentric filling or discharge are composed of two parts, the symmetrical component and the non-symmetrical component referred to as the patch load in EN 1991-4 (BSI, 2006), which shall be taken to act simultaneously on the wall of a silo. The symmetrical component consists of horizontal pressure p_h and vertical friction p_w on the wall, which are given by Eqs. (1)–(4) for the filling stage, where the subscript f indicates filling stage.

For $2.0\le h_c/d_c$,

$$p_{hf}(z)=\gamma K z_0\left[1-\exp\left(-\frac{z}{z_0}\right)\right]. \tag{1}$$

For $0.4<h_c/d_c<2.0$,

Table 1 Geometries of the example silos with capacities of 30 000–60 000 m^3

No.	Geometry of silo	Diameter, d_c (m)	Height, h_c (m)	Slenderness, h_c/d_c	Capacity (m^3)
SILO1	Very slender	20	95.49	4.77	30 000
SILO2	Slender	25	81.49	3.26	40 000
SILO3	Slender	30	70.73	2.36	50 000
SILO4	Intermediate slender	35	51.97	1.49	50 000
SILO5	Squat	45	31.44	0.70	50 000
SILO6	Retaining	60	21.22	0.35	60 000

$$p_{\mathrm{hf}}(z)=\gamma K z_0\left\{1-\left[\left(\frac{z-h_0}{z_0-h_0}\right)+1\right]^n\right\}. \tag{2}$$

For $h_c/d_c \le 0.4$,

$$p_{\mathrm{hf}}(z)=\gamma K(1+\sin\phi_r)z. \tag{3}$$

The vertical friction p_w is defined based on the following common relation:

$$p_{\mathrm{wf}}(z)=\mu p_{\mathrm{hf}}(z). \tag{4}$$

In Eqs. (1)–(4), z is the depth below equivalent surface, γ and K are the unit weight and lateral pressure ratio of the particulate solid, respectively; μ is the wall friction coefficient for solid sliding on the vertical wall; $z_0=r/(2K\mu)$ for circular silos, and r is the radius of silo; h_0 is the depth below the equivalent surface to the lowest point on the wall that is not in contact with the stored solid of the top pile, while $h_0=r\tan(\phi_r)/3$ for a symmetrically filled circular silo with top pile. $n=-(1+\tan\phi_r)/(1-h_0/z_0)$, and ϕ_r is the angle of repose of the particulate solid of conical pile.

The symmetrical discharge pressures p_{he} and p_{we} are determined by the simple overpressure factors C_h and C_w as follows:

$$p_{\mathrm{he}}(z)=C_h p_{\mathrm{hf}}(z), \tag{5}$$

$$p_{\mathrm{we}}(z)=C_w p_{\mathrm{wf}}(z), \tag{6}$$

where C_h and C_w are the discharge factor for horizontal pressure and frictional traction, respectively. The factors are in the range between 1.0 and 1.15 determined by the silo slenderness and action assessment class.

When it comes to large eccentricity discharge, the wall pressures are calculated by the definition of three zones called the flowing zone, the adjacent zone, and the static zone, which are based on a parallel-sided flow channel throughout the height of the silo wall. The size of flow channel is defined in terms of the ratio of flow radius to silo radius by $k_c=r_c/r$, and three specific channel radii are proposed, $k_c=0.25$, 0.40, and 0.60, to account for the eccentricity of the channel and related wall solid pressure. The horizontal pressure p_{hce} in the flowing zone is given by

$$p_{\mathrm{hce}}=\gamma K z_{\mathrm{oc}}\left[1-\exp\left(\frac{-z}{z_{\mathrm{oc}}}\right)\right], \tag{7}$$

where z_{oc} is the Janssen characteristic depth for a flow channel. The horizontal pressure p_{hse} in the static zone is equivalent to p_{hf} in the concentric filling process, and the pressure p_{hae} in the adjacent zone is determined by the simple relation $p_{\mathrm{hae}}=2p_{\mathrm{hf}}-p_{\mathrm{hce}}$. The frictional traction in the zones is also defined according to the common relation $p_w=\mu p_h$. The eccentric flow channel wall contact angle, which is proved to be independent of slenderness of the silo but determined by the radius ratio k_c, is approximately equal to 11.06°, 18.64°, and 30.56° for $k_c=0.25$, 0.40, and 0.60, respectively. For details of the distribution of large eccentric discharge pressure, please refer to EN 1991-4 (BSI, 2006).

In the case of large eccentricities of filling, the effect of the asymmetry of the normal pressures in inducing vertical forces in the silo wall is considered, which is fulfilled by adding the vertical wall pressures to those evaluated for symmetrical filling with a fill level corresponding to filling symmetrically to the highest wall contact. The expressions for determination of the asymmetry vertical pressure were given by EN 1991-4 (BSI, 2006), and not cited here for brevity.

Before pressures on the vertical wall of a silo can be evaluated, the relevant properties of the stored particulate solid have to be made clear. For commonly encountered bulk solids in industry such as cement clinker, the characteristic values of material properties are: $\gamma=18$ kN/m^3, $K=0.38\times1.31=0.498$, $\mu=0.46\times1.07=0.492$, and $\phi_r=47°$ (excerpted from Table E.1, BSI, 2006). The characteristic values K and μ are determined by multiplying or dividing the corresponding mean values by the conversion factors a: $K=a_K K_m$ and $\mu=a_\mu\mu_m$. When a limit state verification is sensitive to the variability of a material property, upper and lower characteristic values of the material property should be taken into account according to BSI (2002a; 2002b; 2006). The following two load cases are also proposed to be considered in the buckling assessment of silos by EN 1991-4 (BSI, 2006): (a) load case I, maximum frictional pressures with corresponding horizontal wall pressures, plus patch loads; (b) load case II, maximum horizontal

wall pressures with corresponding frictional pressures. It is suggested by the results from Song and Teng (2003) that load case I is slightly more detrimental than load case II. As a result, K and μ are chosen the upper values resulting in maximum friction with corresponding horizontal wall pressures.

3 Numerical analysis procedure

3.1 FE model

The buckling behavior of steel silos subject to solids pressure is investigated using the commercial general purpose FE computer package ANSYS (ANSYS, 2008). The eight-node quadratic isoparametric shell element SHELL93 involving both the bending and membrane effect is used to discretize the shell wall. Each FE node has six degrees of freedom (DOFs), including translations in the nodal x, y, and z directions and rotations about the nodal x, y, and z axes. The FE model is defined in the cylindrical coordinate system (i.e., x-radial direction, y-circumferential direction, and z-meridional direction), including the definition of silo geometries and output results, unless it is specifically stated otherwise. The results are from the top layer of the shell element, in which the meridional displacement u and the circumferential displacement v are specified as positive in the coordinate positive directions z and y, and the radial displacement w as positive outwardly normal to the shell surface. The symmetric distribution of solid pressure permits half of the silo to be modeled (Song and Teng, 2003; Sadowski and Rotter, 2011b). As a result, the FE half model, obtained by cutting the shell wall vertically across a diametrical plane, is used in the following analysis.

The base strake of the silo wall is commonly anchored to the rigid bottom plate in most practical situations. For simplification, the bottom plate is not included here in the numerical model, and all translational and rotational degrees of freedom ($U_{x,y,z}$=0, $\mathrm{Rot}_{x,y,z}$=0) at the bottom edge of silo wall are restrained as boundary conditions. The roof and wind girder at the top of silo are also omitted in the numerical model, so only a cylindrical shell is modeled. The radial and tangential translational restraints ($U_{x,y}$ =0) are applied to the silo top to simulate the influence of the roof and the wind girder, as they provide realistic restraints of out-of-round deformation for the silo top. The symmetric boundary condition (U_y=0, $\mathrm{Rot}_{x,z}$=0) is correspondingly imposed in both meridional cut edges of the FE model. The FE mesh and restraint condition for boundary edges of the silo wall are shown in Fig. 2.

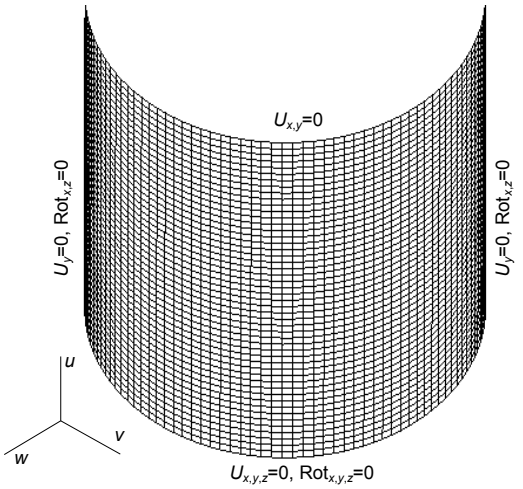

Fig. 2 FE half model of circular steel silo

The material of the silo wall is assumed to be isotropic elastic-perfectly plastic with properties typical of steel (grade S355): an elastic modulus E of 2.1×10^5 N/mm^2, a Poisson's ratio v of 0.3, and a characteristic value of yield strength f_{yk} of 355 N/mm^2 (BSI, 2007a).

Another geometrical parameter which has been proved to have a considerable effect on the buckling behavior of a circular steel silo is the weld depression imperfection arising from the fabrication process of the silo wall. In the present analysis, the assumed shapes of weld depression (type A) are adopted and introduced to the FE model, such as are proposed by Rotter and Teng (1989). The height of a normal strake is assumed to be 3.0 m. For the example silos, such as SILO4 in Table 1, 17 circumferential weld depression imperfections along the wall height are modeled, in which areas in the vicinity of the weld depression are discretized with denser meshes.

3.2 Types of buckling analysis

The limit state of buckling should be taken as the condition in which all or part of the structure suddenly develops large displacements normal to the shell

surface, caused by loss of stability under compressive membrane or shear membrane stresses in the shell wall, leading to inability to sustain any increase in the stress resultants, possibly causing total collapse of the structure. For the determination of load carrying capacities when checking the buckling limit state, the following six types of buckling analysis, which are also recommended by EN 1993-1-6 (BSI, 2007a), are carried out for the numerical investigation:

1. LBA—linear elastic bifurcation analysis of the perfect silo;

2. GNA—geometrically nonlinear elastic analysis of the perfect silo;

3. MNA—geometrically linear and materially nonlinear analysis of the perfect silo;

4. GMNA—geometrically and materially nonlinear analysis of the perfect silo;

5. GNIA—geometrically nonlinear elastic analysis of the imperfect silo;

6. GMNIA—geometrically and materially nonlinear analysis of the imperfect silo.

For buckling analyses, the recommended partial factor γ_f of solids pressure is taken as 1.5 by EN 1991-4, and the partial safety factor γ_{M1} for the resistance of the shell wall to stability is recommended for silos as 1.1 (BSI, 2007b), giving an overall safety amplification factor 1.5×1.1=1.65 applied to the design values for the relevant load case. This safety factor of 1.65 provides a valuable reference for the load proportionality factor against which nonlinear numerical analyses may be estimated to obtain a realistic measure of safety of the designed structure.

4 Determination of buckling resistance of silo structure

For the buckling analyses of shell structures, two kinds of buckling are defined according to the structural equilibrium path. These are well known as the linear bifurcation buckling and nonlinear snap-through buckling. The linear buckling analysis predicts the theoretical buckling strength (the bifurcation point) of an ideal linear elastic structure, while in the nonlinear buckling analysis, the critical buckling is obtained by following the structural load-displacement full course responses for both geometrically perfect and imperfect models.

The load-displacement curves, which are calculated by selecting the monitoring node at the critical buckling point, may be obtained for various buckling analysis types. There are also two types of fundamental equilibrium path (Fig. 3) on which the critical buckling factor λ_{cr} is based: (1) the maximum load factor λ_{cr1}: load displacement curves predict a distinct maximum load factor followed by a descending path; (2) the load factor λ_{cr2} corresponding to the largest tolerable deformation, where this occurs during the loading path before reaching a maximum load factor. The tolerable global deflection w (radial displacement) for a steel silo is recommended to be taken as $H/50$ (BSI, 2007b), where H is the height of the structure measured from the foundation to the roof. As the shell structure always buckles accompanying the geometric imperfections or plasticity, only nonlinear buckling results are adopted to estimate the buckling strength of the example silos. The load carrying capacity of buckling is characterized by the buckling resistance factor λ_R, which is proposed by EN 1993-1-6, when checking the buckling limit state. As a result, the critical buckling factor from the minor values of λ_{cr1} and λ_{cr2} is taken as the buckling resistance factor λ_R of the example silos, which is a dimensionless parameter indicating the ratio of the designed load on silo structure to buckling strength.

It is well known that buckling strength of a silo structure is closely correlated with the mesh size of the silo wall in the FE model. The lowest linear critical buckling load factor λ_{cr} of the example silos is obtained using different numbers of elements in both circumferential and axial directions, as is plotted in Fig. 4. When the size of shell elements of the silo wall decreases from 4.0 m×4.0 m (circumferential size and axial size) to 1.0 m×1.0 m, the critical buckling factor gradually converges at the constant load factor for all example silos. The discrimination of critical buckling factors between element sizes 4.0 m×4.0 m and 1.0 m×1.0 m is about 3%–6% for the example silos, and that is reduced to 1%–2% for results between element sizes 2.0 m×2.0 m and 1.0 m×1.0 m, while the results from element sizes 1.5 m×1.5 m and 1.0 m×1.0 m make no difference. It is concluded that the quadratic element type SHELL93 with midside nodes is applicable and highly effective in modeling the buckling behavior of silo structures subject to

solid pressure. It is certainly preferable to keep the element sizes to less than 1.5 m×1.5 m in order to obtain the accurate buckling factors.

5 Buckling behavior under concentric discharge

For various reasons, buckling analyses of silo walls are carried out in a diversity of forms known as the uniform thickness, the stepwise thickness, and the tapered thickness. Although the stepped wall thickness is commonly adopted in practical fabrication of a silo wall for ease of construction, the tapered wall thickness for the example silos is also preferred in this paper because of its convenience for numerical modeling and better structural performance, which would bring about an effectively continuous taper and avoid discontinuity of wall stiffness compared to the stepped wall thickness. For the tapered wall thickness, the equivalent thickness t_{eq} is determined by the wall thickness at the uppermost t_{top} and at the downmost t_{bot}, and in the form of $t_{eq}=(t_{top}+t_{bot})/2$.

5.1 Stress and deformation distribution

The meridional compressive stress has been recognized as the main cause of many buckling failures of a silo structure. It is very helpful to make clear the distribution of stress and deformation on the silo wall for a better understanding of buckling behavior. In this section, the results of stress and deformation from the LA are presented for the example silos subject to concentric discharge pressure, and are shown in Figs. 5 and 6. The vertical axes in the plotting represent the depth z from the bottom normalized by the height h_c of the silo wall, while the horizontal

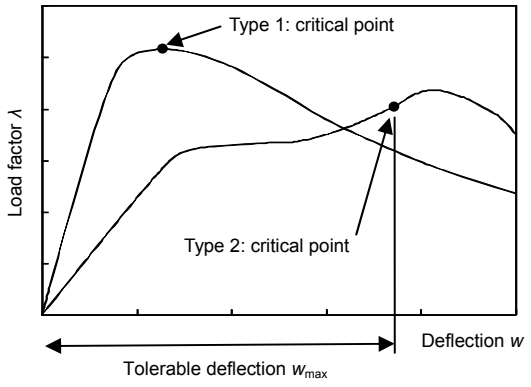

Fig. 3 Determination of critical buckling factor λ_{cr} of silo structure

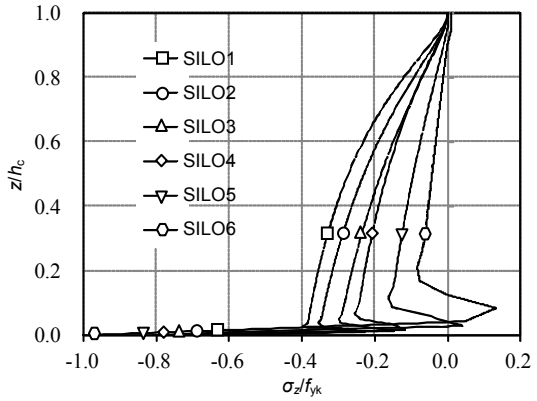

Fig. 5 Distribution of meridional stress of example silos along the wall height

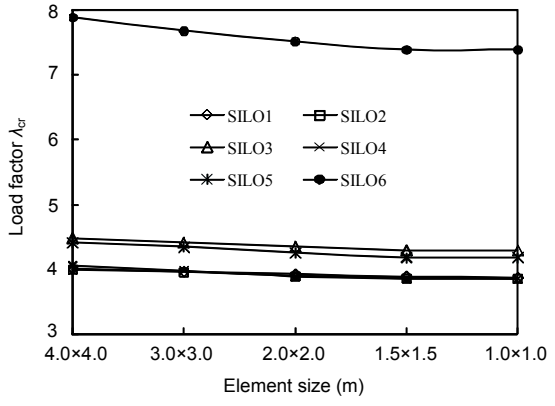

Fig. 4 Variation of critical load factor with mesh density of example silos

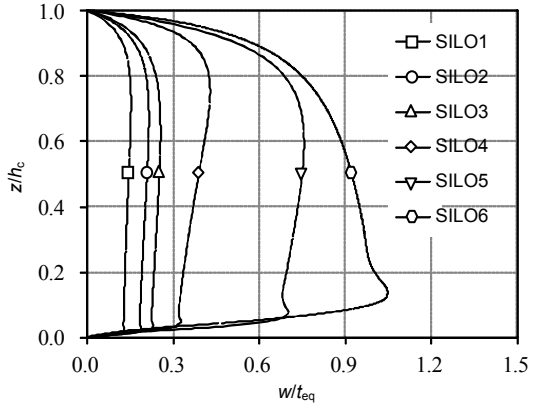

Fig. 6 Distribution of radial displacement of example silos along the wall height

axes represent the meridional stress component σ_z normalized by the material yield stress f_{yk} and the radial displacement w normalized by the equivalent thickness t_{eq} of the silo wall, respectively.

It is shown in Fig. 5 that the meridional stress is compressive along the wall height and increases gradually from top to bottom, while the inflection point is induced at a critical height z_{cr} due to the restraint effect of rigid base. The stress magnitude $\sigma_{z,cr}$ at critical height z_{cr} is significantly reduced by the negative moment, which is much more obvious for a small slenderness silo and tensile meridional stress is even discovered in the zone adjacent to critical height z_{cr} for retaining silo SILO6. The critical height z_{cr} and the meridional stress $\sigma_{z,cr}$ vary significantly with the aspect ratio of example silos and the compressive stress reaches its maximum value $\sigma_{z,max}$ at the bottom of the silo wall. The critical height z_{cr} is discovered to increase with the decrease of silo slenderness, which is about $0.03h_c$ for example SILO1 and $0.08h_c$ for example SILO6. The stress ratio $\sigma_{z,cr}/\sigma_{z,max}$ is found to increase with the increase of silo slenderness, which is about 0.62 for example SILO1 and −0.14 for example SILO6. It is concluded that the meridional stress σ_z is highly unevenly distributed along the height of the silo wall due to the pressure distribution and boundary effect, especially in the area adjacent to the wall bottom.

The radial displacement plotted in Fig. 6 is shown to increase from top to bottom, and reaches its maximum value w_{max} at the critical height z_{cr} and vanishes at the bottom. The maximum radial displacement is closely dependent on the slenderness of example silos, and increases significantly with the decrease of silo slenderness. The distribution is exactly consistent with that of meridional stress shown in Fig. 5. In addition, the circumferential distribution of the meridional stress and radial displacement are axisymmetric, as can be easily concluded from the symmetry of silo structure and wall pressure.

5.2 Critical buckling factor and load displacement full course

In this section, buckling behavior in concentric discharge is first investigated for the case of steel silos with tapered wall thickness. Both linear bifurcation and nonlinear buckling analyses are carried out. The critical buckling load factors are listed in Table 3 for various slendernesses of example silos in each buckling analysis. This shows that the GMNIA analysis gives out the minimum buckling factors from all proposed buckling analysis types for all example silos. The critical buckling factor λ_{cr} in GMNIA analysis is slightly larger than and satisfies the requirement of the overall safety factor 1.65, which is consequently taken as the buckling resistance factor λ_R of the example silos. The designed wall thickness distribution corresponding to the critical buckling factor λ_{cr} in Table 3 and used for buckling analysis below is given in Table 4.

The load-displacement curves are plotted in Fig. 7 for various types of buckling analysis of example silos. The curves are calculated by selecting the monitoring node in the maximum wall deflection at the critical buckling point. The vertical axis is the dimensionless load factor λ being applied to the design value of solids pressures, while the horizontal axis represents the out-of-plane radial displacement normalized by the equivalent thickness t_{eq} of the silo wall listed in Table 4. The load-displacement curves are highly nonlinear which means the principle of superposition appropriate for the linear structure turns out to be inapplicable for the thin-walled steel silos under concentric solid pressure. Furthermore, the load-displacement curves predict a distinct maximum load followed by a descending path, in which the maximum load is taken as the critical buckling point λ_{cr} for the equilibrium path.

Fig. 7 shows that the load factor λ initially increases linearly with the increasing radial displacement in the range of a certain critical w_{cr} before the critical point λ_{cr} is reached, and the critical radial displacement w_{cr} corresponding to the critical buckling factor λ_{cr} varies greatly for different slendernesses of example silos, in which the critical displacement w_{cr} increases apparently with the decrease of the slenderness of silo. For instance, the critical displacement w_{cr} for SILO1 (very slender silo) is about 0.4 times (12 mm) the even thickness t_{eq}, but the value is approximately equal to 2.1 times (58.8 mm) t_{eq} for SILO6 (retaining silo) in the GMNIA analysis (Fig. 7d). In other words, the slope to the vertical axis of the load-displacement curves in the linear stage is much larger for small slenderness of silo than that for large slenderness of silo. While it is even more apparent in other types of buckling analysis, the critical

Table 3 Critical buckling factors for example silos from proposed buckling analysis types under concentric discharge

No.	Geometry of silo	Critical buckling factor, λ_{cr}					
		LBA	GNA	MNA	GNIA	GMNA	GMNIA
SILO1	Very slender	3.87	4.34	2.23	3.59	2.12	1.77
SILO2	Slender	3.78	4.13	2.22	3.72	2.03	1.73
SILO3	Slender	4.22	4.37	2.38	3.98	2.10	1.79
SILO4	Intermediate slender	4.04	4.17	2.11	3.96	1.91	1.68
SILO5	Squat	4.71	4.62	1.93	4.47	1.82	1.71
SILO6	Retaining	7.43	7.22	1.82	7.05	1.69	1.66

Table 4 Designed wall thickness and RCS index of example silos under concentric discharge

No.	Diameter, d_c (m)	Height, h_c (m)	Slenderness, h_c/d_c	t_{top} (mm)	t_{bot} (mm)	t_{eq} (mm)	Capacity (m^3)	Steel consumption (m^3)	RCS
SILO1	20	95.49	4.77	6.0	54.0	30.0	30000	180.00	166.67
SILO2	25	81.49	3.26	6.0	56.0	31.0	40000	198.40	201.61
SILO3	30	70.73	2.36	6.0	60.0	33.0	50000	220.00	227.27
SILO4	35	51.97	1.49	6.0	56.0	31.0	50000	177.14	282.26
SILO5	45	31.44	0.70	6.0	44.0	25.0	50000	111.11	450.01
SILO6	60	21.22	0.35	4.0	52.0	28.0	60000	112.00	535.71

RCS: ratio of capacity to steel consumption

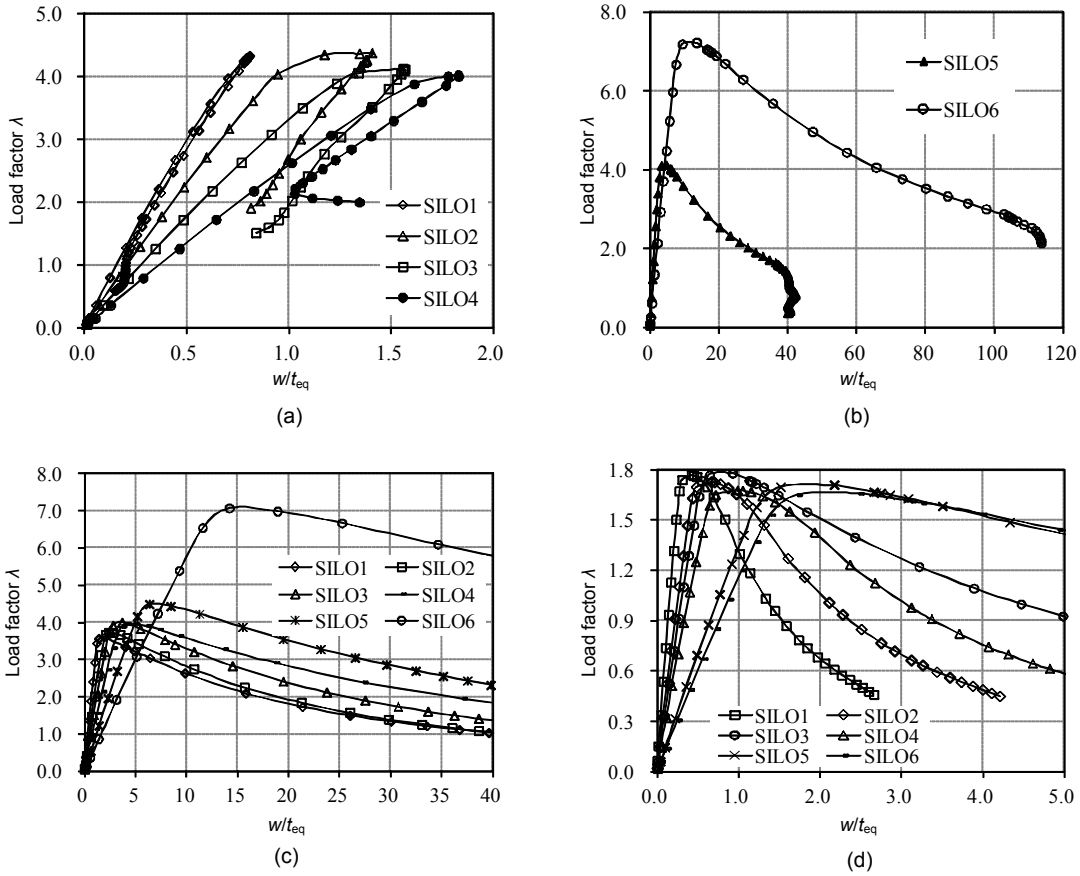

Fig. 7 Typical load-displacement curves of example silos for various types of buckling analysis
(a) & (b) GNA; (c) GNIA; (d) GMNIA

displacement w_{cr} for SILO1 in the GNA analysis is about 0.81 times (24 mm) the even thickness t_{eq}, and the value is amplified to be about 13.6 times (380 mm) t_{eq} for SILO6 (Figs. 7a and 7b). It indicates that the silo with smaller slenderness is superior in structural ductility and plasticity to that of the one with larger slenderness, and the retaining silo or squat silo is preferred in structural design for practical purposes. When the critical buckling point λ_{cr} is passed, the sudden descent of the load factor is clearly found with a large radial deflection increase, which indicates the shift of the equilibrium path from the prebuckling to the postbuckling stage.

In other types of nonlinear buckling analyses such as MNA and GMNA, the equilibrium paths shown by the load-displacement curves are also characterized by one of the two curves plotted in Fig. 3, and similar conclusions can also be drawn, so they are not given here for brevity.

5.3 Buckling modes

The buckling modes of example silos for LBA analysis are plotted in Fig. 8 corresponding to the lowest buckling eigenvalue, which shows that the structural deformations are axisymmetrical and mainly occur in the form of harmonic waves in the axial direction in the middle region of the silo wall. The number of harmonic waves caused by the meridional compression is closely related to the slenderness of the silo, i.e., the number increases with the increase of the silo slenderness and decreases with the decrease of the silo slenderness. The deformations from linear buckling analysis are far different from that predicted by the LA, in which the outward radial deflections increase with the depth from the top, and obtain their maximum value at the height adjacent to the silo bottom.

The nonlinear buckling deformations which are taken from the critical buckling point are very different from the buckling mode given by the linear bifurcation (LBA) result. The buckling deformations predicted by the GNA, MNA, and GMNA analyses are similar, where the radial deflections increase with the depth and the maximum deflections occur just adjacent to the bottom of the silo wall. The buckling modes from the GNA, MNA, and GMNA analyses shift into the well-known elephant-foot deformations at the bottom part of the shell wall, which agree well with the deformations evaluated by the LA analysis in Fig. 6. In such a case, the deformation of thin-walled example silos is plastic buckling at the bottom induced by the meridional compressive stress due to the vertical friction acting on the internal surface of the silo wall.

The buckling modes from the GNIA and GMNIA where the weld imperfection is taken account of are also similar, and show other different buckling deformations from those of geometrically perfect models. The results from the GMNIA are plotted in Fig. 9 for the example silos studied, which reveal that the structural deformations mainly occur in the form of harmonic waves in the axial direction throughout the whole height of the silo wall and the number of harmonic waves is almost identical to that of the weld imperfections. In addition, the modes are also axisymmetrical plastic buckling and the elephant-foot deformations at the bottom part of the shell wall also occur in spite of the interactive effect with the multi weld depressions. It suggests that the geometric weld imperfections induced during fabrication should be taken into consideration for the structural design of steel silos.

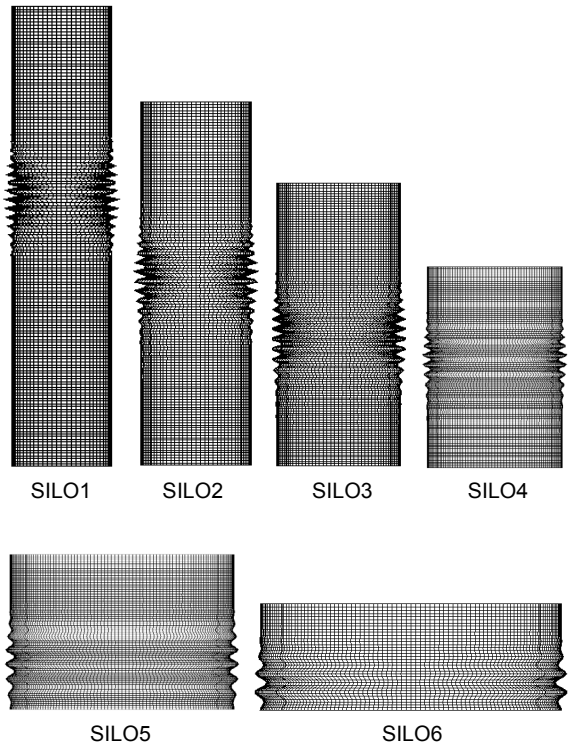

Fig. 8 Buckling modes of the example silos in LBA

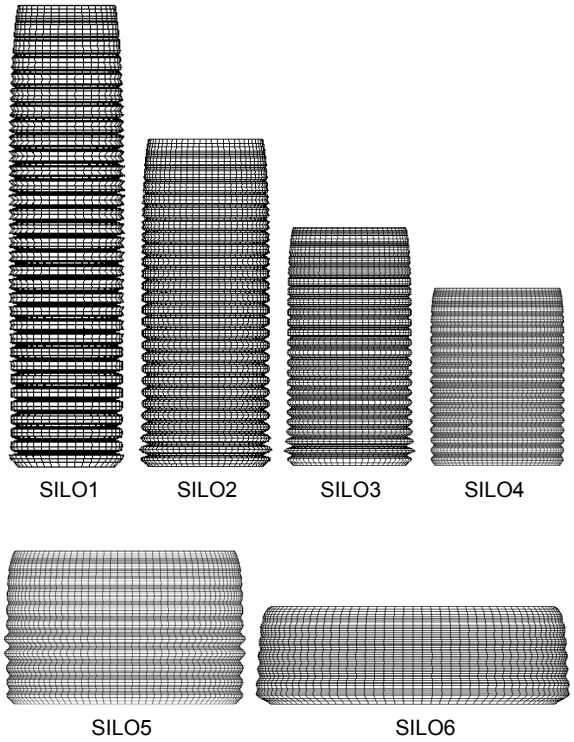

Fig. 9 Buckling modes of the example silos in GMNIA

5.4 Effects of nonlinearity and imperfection

The nonlinear effect proves to have much influence on the buckling behavior of steel silos. The geometrical nonlinear effects on various slendernesses of example silos are plotted in Fig. 10 by the ratio of GNA load factor λ_{cr1} to LBA load factor λ_{cr2} listed in Table 3. This reveals that geometrical nonlinearity is beneficial for steel silos with large slenderness but somewhat harmful for steel silos with small slenderness. The buckling factor λ_{cr} for a very slender silo (SILO1) increases by about 12% for the beneficial effect of geometrical nonlinearity, but it decreases by about 3% for retaining silo (SILO6) for the harmful effect of geometrical nonlinearity. As steel silos are typical kinds of thin-walled structure, and large deflections always occur with the buckling of a structure, geometrical nonlinearity should therefore be taken into account in buckling analysis of steel silos.

The material nonlinear effect is also plotted in Fig. 10 by the ratio of MNA, GMNA or GMNIA load factor λ_{cr1} to LBA, GNA or GNIA load factor λ_{cr2} listed in Table 3, which reveals that material nonlinearity is strong and detrimental to buckling behavior of all slendernesses of example silos, resulting in a decrease of buckling resistance for both perfect and imperfect models. The conclusion agrees well with that from Iwicki *et al*. (2014) and that from Song and Teng (2003). The detrimental effect of material nonlinearity brings about a decrease of buckling load factor by about 50%–80%, which is much more unfavorable for steel silos with small slenderness than those with large slenderness. For instance, the buckling load factor reduced by about 51% for a very slender silo (SILO1) arising from the effect, but the factor reduced by about 78% for the retaining silo (SILO6). It is indicated that the effect of material plasticity is extremely powerful and plays a decisive role in nonlinear buckling analyses for every slenderness of large steel silo. As a result, material with higher yield strength is recommended in the buckling design of large steel silos, where the current conclusions show a considerable discrepancy with those drawn from investigations of small capacity of steel silos (Sadowski and Rotter, 2011b).

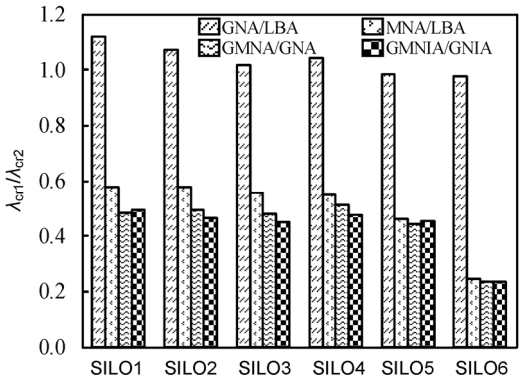

Fig. 10 Geometrical and material nonlinear effects in buckling analysis

The weld imperfection effect is shown in Fig. 11 by the ratio of GNIA or GMNIA load factor λ_{cr1} to GNA or GMNA load factor λ_{cr2} listed in Table 3, which reveals that weld imperfection is detrimental to buckling behavior of all slendernesses of example silos. The detrimental effect is more serious for slender silos than squat silos, where the buckling load factor reduced by about 17% for the very slender silo (SILO1), but the factor reduced only by about 3% for retaining silo (SILO6). The reasons are explained in what follows: since the strake height for construction

of the vertical wall of the silo is assumed to be the invariant value of 3 m, the number of circumferential weld imperfections simulated in the slender silo is much greater than that in the squat silo. For instance, there are 31 circumferential weld imperfections along the wall height modeled for the very slender silo (SILO1), whereas six merely weld imperfections are modeled for the retaining silo (SILO6). The interaction between the neighboring circumferential weld imperfections further reduced the buckling strength and this is more obvious for slender silos with more weld imperfections. It suggests that the weld imperfections should be incorporated in the numerical models and the magnitude be reduced in the fabrication of a silo wall to improve the buckling resistance of the structure.

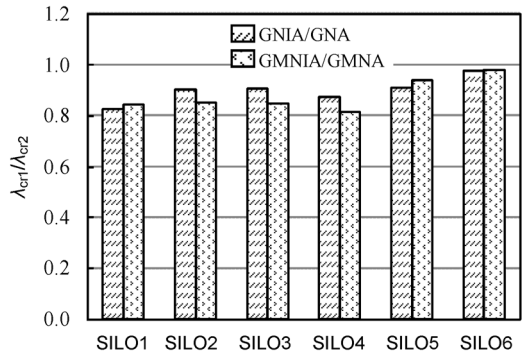

Fig. 11 Weld imperfection effects in buckling analysis

5.5 Designed wall thickness and steel consumption index

Steel silos with large capacity are usually used for storage of huge quantities of granular solids, and the consumption of materials in the construction of some silo walls can be as large as thousands of tons. The amount of material in steel silos may differ greatly depending on the designers. The index called the ratio of capacity to steel consumption (in volume) (RCS) is initially defined by Eq. (8), which provides a useful parameter in the design of steel silos.

$$\mathrm{RCS}=\frac{\text{Capacity of steel silo}}{\text{Steel consumption of silo wall}}. \tag{8}$$

This RCS index of a steel silo is a dimensionless parameter indicating the material efficiency of the storage of steel silos.

The wall thicknesses satisfying the buckling requirement of silo design stipulated by the Eurocode are listed in Table 4 together with the RCS index. The top thickness of the tapered wall is commonly encountered as a thin 4 mm or 6 mm, but the bottom thickness is much greater, and that for the retaining silo wall can even be as much as 60 mm, which undoubtedly adds difficulty to the fabrication and flexure of the silo wall. For the example silos above, the steel in a silo wall ranges from about 112 m^3 to 180 m^3 with the variation of slenderness from retaining to very slender, equivalent to a mass between approximately 880 t and 1400 t.

The variation of the RCS index with the slenderness of steel silo is plotted in Fig. 12, which shows that the RCS index increases rapidly with the decrease of silo slenderness. In other words, the storage efficiency of a steel silo improves greatly with the slenderness varying from slender silo to retaining silo. For instance, the RCS index for the very slender silo (SILO1) is about 167, but the value for the retaining silo (SILO6) is about 536, a factor of approximately 3.2. Similarly, for steel silos with a capacity of 50000 m^3, the RCS index for SILO5 with a slenderness of 0.7 is approximately 1.6 times that of SILO4 with slenderness of 1.49. It suggests that silos with small slenderness such as squat and retaining silos are to be preferred in steel silo structural design.

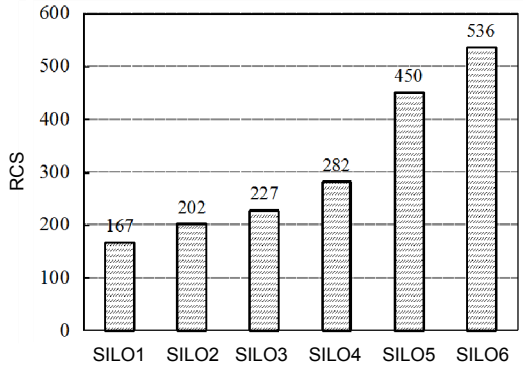

Fig. 12 Relationship of RCS index with slenderness of example silos

5.6 Discharge patch load effect

It is specified (BSI, 2006) that the patch load shall be used to represent accidental asymmetries of loading during discharge. From the viewpoint of safe

design, the patch load position h_p should be placed anywhere over the height of the silo wall, and buckling of the silo should be based on the most unfavorable position of the patch load. The effect of patch load position on buckling behavior of example silos is investigated, and this shows that the patch load is unfavorable to buckling and results in a decrease of about 5%–25% of the buckling factor. The most unfavorable position of the patch load is approximately 0.6 time of the height h_c for the example silos, which is adopted for the evaluation of patch load effect in this section.

The effect of patch load on buckling resistance in the GMNIA is plotted in Fig. 13 by the ratio of buckling resistance λ_{cr1} in the case of patch load to λ_{cr2} under concentric solid pressure, which shows that the effect is unfavorable for buckling resistance of all slendernesses of example silos. Nevertheless, the detrimental effect is much more serious for silos with large slenderness than those with small slenderness. The buckling resistance λ_{cr1} is reduced by about 9% for the very slender silo (SILO1), whereas the detrimental effect is very small for the retaining silo (SILO6), with only a decrease of about 1% compared to λ_{cr2}. The recommendation by EN 1991-4 that the effect of patch load on squat and retaining silos can be neglected is shown to be reasonable according to the numerical evaluation. In such cases, the RCS index is also slightly reduced by less than 10% for slender silos due to the limited effect of patch load, even in case of the largest eccentricity of $0.25d_c$, and it remains almost invariable for squat and retaining silos. The variation of RCS with slenderness of example silos is similar to that obtained in the load case of concentric discharge, and thus is not given again.

5.7 Effect of boundary condition

In the preceding analysis, the base strake of silo wall is assumed to be anchored to the rigid bottom plate and the clamped boundary condition ($U_{x,y,z}$=0, $\mathrm{Rot}_{x,y,z}$=0) is used at the lower edge of the silo wall. However, the restraints of rotational degrees of freedom ($\mathrm{Rot}_{x,y,z}$=0) at the bottom edge of the silo wall could not be effectively achieved for many practical considerations, such as the limited rigidity of the bottom plate, and what is more important, full welds between the base strake and the bottom plate are especially difficult to achieve. The simply supported boundary condition ($U_{x,y,z}$=0) is considered and the buckling results are compared with those from the clamped boundary condition.

The effect of boundary condition on buckling resistance in the GMNIA is plotted in Fig. 14 by the ratio of buckling resistance λ_{cr1} under simply supported to λ_{cr2} under a clamped boundary condition. It reveals that the variation of boundary condition from clamped to simply supported has a limited influence on buckling strength of example silos, but is more marked for squat silos than for slender silos. The variation of boundary condition from clamped to simply supported results in a decrease of buckling strength by about 9% for SILO6, but only induces a decrease of about 1% for SILO1. It is concluded that the effect of boundary condition should be incorporated in the numerical models for buckling analysis, especially for the squat and retaining silos.

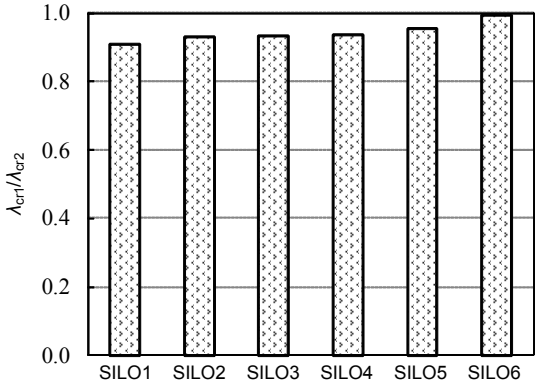

Fig. 13 Effect of patch load on buckling resistance in GMNIA

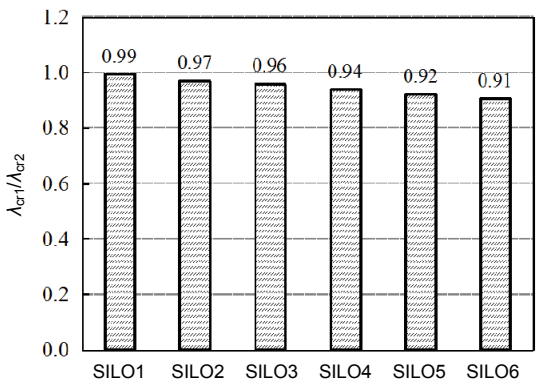

Fig. 14 Effect of base rigidity on buckling resistance of example silos

5.8 Stepwise thickness of silo wall

The preceding investigation is carried out by assuming that the wall of the steel silo is tapered from the bottom to the top. This assumption is theoretically ideal, whereas silo strakes with different thicknesses are joined with welds to construct the complete structure in most practical circumstances, forming the so-called stepped wall thickness. Therefore, it is of great importance to perform a buckling analysis of silo structures with stepped wall thickness. The buckling behavior of the retaining silo (SILO6) with stepped wall thickness and with the minimum number of weld depressions is taken as the representative of the example silos and evaluated in this section. The results will also be compared with that from the tapered and uniform wall thickness under the circumstances that the three types of wall thickness distribution share the same equivalent thickness t_{eq} of 28 mm as determined by the former investigations. In the case of the stepped wall silo, the equivalent thickness t_{eq} is defined in the following form:

$$t_{eq}=\frac{\sum h_i t_i}{\sum h_i}, \tag{9}$$

where h_i and t_i is the height and thickness of the ith wall strake, respectively. For the convenience of comparison, four groups of thickness for stepped wall are designated, as are noted groups A to D in Table 5 together with the distribution of uniform and tapered wall thickness.

The effects of different types of silo wall thickness on buckling resistance are demonstrated in Fig. 15 by the ratio of λ_{cr1} of the silo wall thickness in groups A–E to λ_{cr2} of the tapered thickness in group F predicted in the preceding studies. It indicates that the distribution of wall thickness has much influence on the buckling resistance and buckling mode of the silo structures. The buckling resistance may decrease greatly due to irregular distribution of wall thickness. For thickness distribution in groups A, B, and C, the buckling deformations initially occur in the top several strakes of the silo wall which is relatively thin and vulnerable to deflections compared with other regions. Thus, in such cases the buckling strength of the wall strakes at the lower part is not fully utilized, at about 60%–70% to that of the tapered wall thickness, as is shown in Figs. 15 and 16a. For the uniform wall thickness in group E, the buckling deformation plotted in Fig.16c occurs first at the vicinity of the vulnerable bottom, resulting in a decrease of about half of the buckling resistance compared to that of the tapered wall thickness. For thickness distribution in group D, the buckling deformation is shown in Fig. 16b and arises in wall strakes at the top and bottom simultaneously, and the buckling resistance increases by about 5% due to the favorable wall thickness distribution. As a result, the thickness arrangement of group D is the optimal one of those listed in Table 5. It is concluded that the wall thickness type and its distribution have the most important influence on the buckling modes and buckling strength of steel silos. Under the condition of the same amount of steel used in construction, different schemes for wall thickness arrangement are suggested in buckling design of steel silos to achieve the optimal buckling strength.

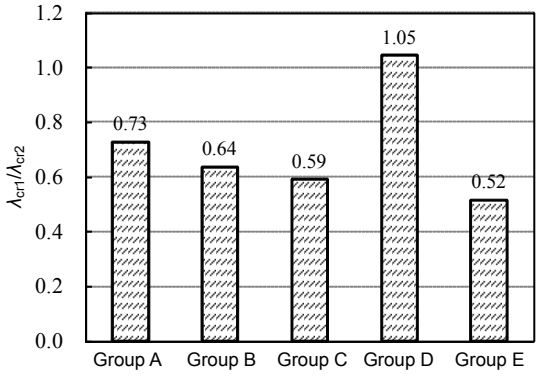

Fig. 15 Effect of thickness distribution on buckling resistance of silos

Table 5 Thickness groups of the retaining silo wall (SILO6) (units: m for h_i; mm for t_i)

Group	$h_1\times t_1$	$h_2\times t_2$	$h_3\times t_3$	$h_4\times t_4$	$h_5\times t_5$	$h_6\times t_6$	$h_7\times t_7$	t_{eq}
A	3.22×4.0	3.0×12.0	3.0×24.0	3.0×30.0	3.0×36.0	3.0×42.0	3.0×50.0	28.0
B	3.22×4.0	3.0×10.0	3.0×20.0	3.0×28.0	3.0×36.0	3.0×44.0	3.0×56.0	28.0
C	3.22×4.0	3.0×8.0	3.0×16.0	3.0×24.0	3.0×36.0	3.0×50.0	3.0×60.0	28.0
D	3.22×6.0	3.0×14.0	3.0×21.0	3.0×28.0	3.0×36.0	3.0×43.0	3.0×50.0	28.0
E	Uniform thickness: t_i=28.0 mm							
F	Tapered wall thickness: t_{top}=4.0 mm; t_{bot}=52.0 mm; t_{eq}=28.0 mm							

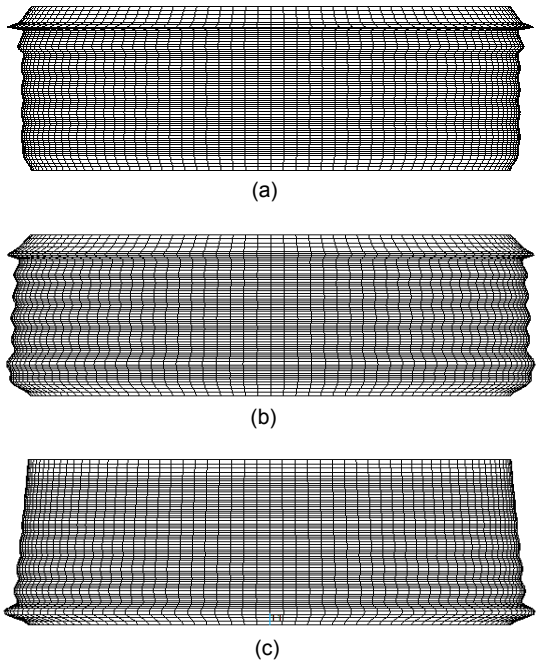

Fig. 16 Buckling modes for various groups of wall thickness distribution
(a) Groups A, B, and C; (b) Group D; (c) Group E

6 Buckling behavior under large eccentricity discharge

In the process of discharging with large eccentricity, the pressures on the wall are determined by assuming a parallel flow channel with circular section. Three typical zones distinguishing the circumferential variation of solid pressure are specified and these are called the flowing zone, the adjacent zone, and the static zone. The eccentric flow channel radius r_c is taken as 0.6 times the silo radius in the following numerical investigation, which has been widely accepted to be the most detrimental size of eccentricity, and also adopted by other researchers (Sadowski and Rotter, 2011c). The eccentric flow channel wall contact angle θ_c has the most impact on distribution zones of solid pressures, with a central angle of about 30.56° for k_c of 0.6 specified in EN 1991-4 (BSI, 2006).

6.1 Stress and deformation distribution

In this section, the results of stress and deformation from a LA are presented for the example silos subject to large eccentric discharge pressure, and are shown in Figs. 17 and 18. It is indicated that the stress and deformation are highly unevenly distributed not only along the wall height but also in the circumferential direction. The maximum meridional stress along the circumferential occurs in the flowing zone, where the vertical distribution of meridional stress σ_z is plotted in Fig. 17 for example silos.

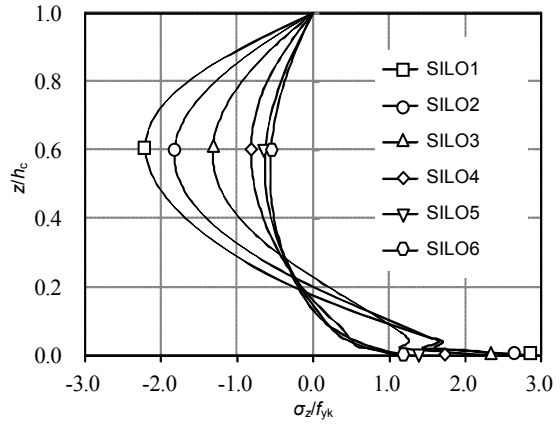

Fig. 17 Distribution of meridional stress of example silos along the wall height

It shows that the meridional stress is compressive in the vertical coordinate z above $0.2h_c$ and becomes tensile for coordinate z below $0.2h_c$ which results from the inflecting bending moment due to the asymmetric distribution of solid pressure. The maximum stress is closely correlated with the slenderness of silos, where the maximum compressive stress $\sigma_{z,max}$ occurs approximately at the critical height z_{cr} of $0.6h_c$, and the maximum tensile stress $\sigma_{z,0}$ occurs at the bottom of the silo wall. The maximum stress increases significantly with the increasing slenderness of example silos, where the maximum compressive stress $\sigma_{z,max}$ and tensile stress $\sigma_{z,0}$ for SILO1 are about $-2.20f_{yk}$ and $2.88f_{yk}$, respectively, and they are about $-0.58f_{yk}$ and $2.16f_{yk}$ for SILO6, respectively. For meridional stress in the adjacent zone, the distribution is quite distinct from that in the flowing zone shown in Fig. 17. The critical height z_{cr} is about $0.55h_c$, and the inflection point is about $0.3h_c$. The meridional stress is tensile at a height range from the top to the inflection point while it is compressive at a height below the inflection point. The maximum compressive and tensile stresses in the adjacent zone are about $-2.96f_{yk}$ and $1.65f_{yk}$ for SILO1, respectively, and they are about $-1.56f_{yk}$ and $0.61f_{yk}$ for SILO6, respectively. The stress distribution in the static zone is similar to

that shown in Fig. 5 and is not given here. It is concluded that the stress distribution of steel silos subject to eccentric discharge pressure is highly non-uniform in both circumferential and meridional directions, which is quite different from the load condition of concentric discharge.

The distribution of radial displacement also shows that the deformation of steel silos is non-uniform in the circumference from the flowing zone to the static zone, where the center of the flowing zone is designated as the circumferential angle θ of −180° in Fig. 18. The maximum radial displacement occurs at about the angle of −130°–−140°, and increases with increasing slenderness of silo. The circumferential variation of deformation is characterized by several waves due to the interval of outward and inward displacements, and the number of waves is dependent on the slenderness of silo which increases with the decrease of slenderness. The variation of waves number is consistent with the circumferential variation of stress on the silo wall.

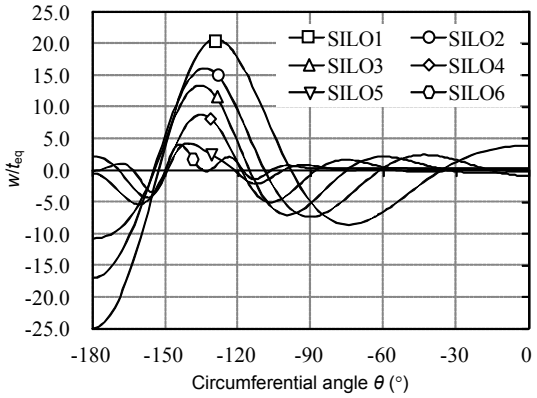

Fig. 18 Distribution of radial displacement of example silos along the circumference

6.2 Buckling modes

The results reveal that the buckling deformations from both the linear and nonlinear buckling analyses are asymmetrical arising from the circumferential and meridional non-uniform distribution of the solid pressures. The buckling deformations from the LBA analysis shown in Fig. 19 occur taking the form of several meridional waves with assorted magnitudes mainly in the middle part of the flowing zone for silos with large slenderness as the very slender silo (SILO1), and the deformed area shifts into its adjacent zone gradually with the decrease of the silo slenderness, such as the retaining silo (SILO6). The deformation in the static zone is nearly invisible compared to that in the flowing zone or adjacent zone. In addition, the deformation transfers to the top area for small slenderness of silo such as the squat and retaining silos, in the form of local buckling, indicating the distinction of buckling modes between the slender silos and the squat silos.

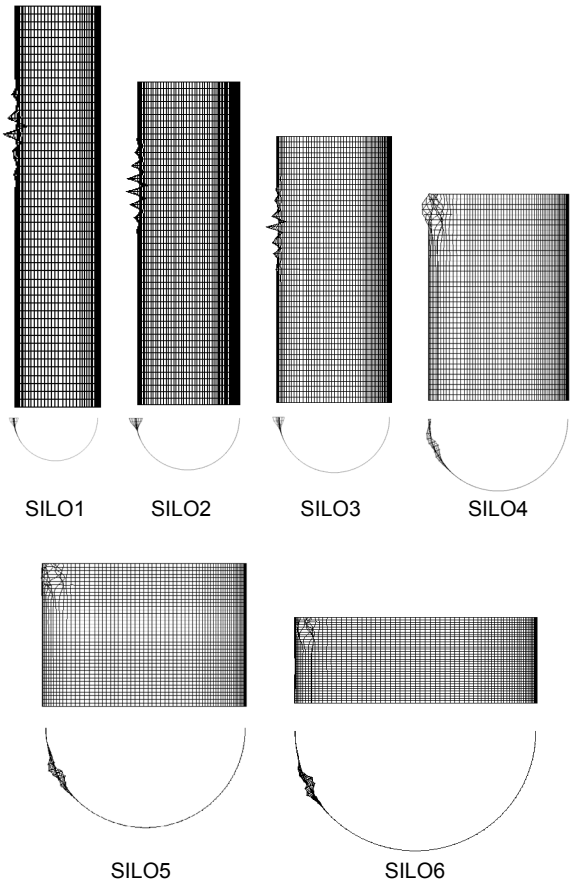

Fig. 19 Buckling modes of the example silos in LBA

The nonlinear buckling deformations corresponding to the critical buckling point occur over nearly all the height of the silo wall, but obtain the maximum value in the middle height for both the perfect (GNA, MNA, and GMNA) and imperfect (GNIA amd GMNIA) models. The deformations in the flowing zone are concave to the center and convex in the adjacent zone deviating from the center. Several circumferential waves with small magnitude are also

seen in the static zones. The "elephant's failure" modes, which have been the signs of plastic deformation of silos under eccentric solid pressure, are not clearly observed in the GMNA and GMNIA with consideration of material nonlinearity. The buckling modes of example silos in the GMNIA are plotted in Fig. 20.

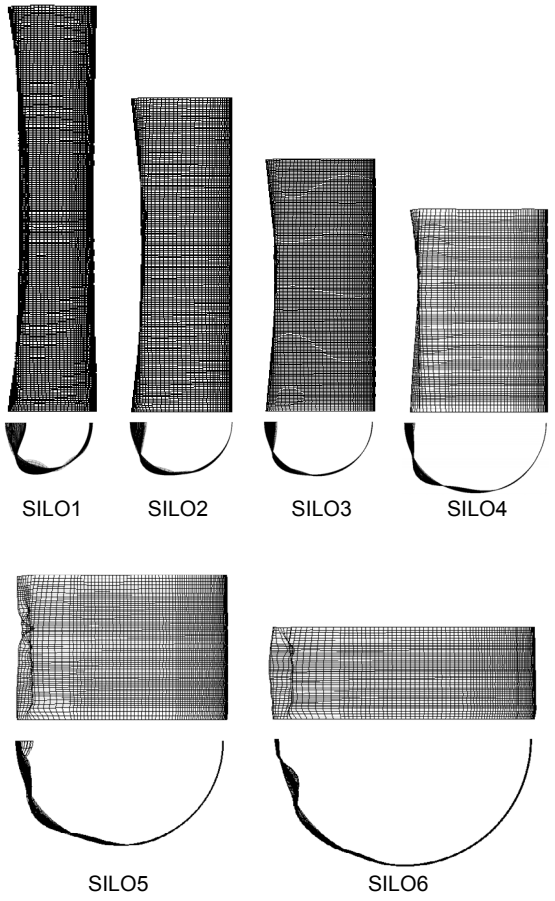

Fig. 20 Buckling modes of the example silos in GMNIA

In addition, the distribution of weld imperfections have not as much impact on the buckling modes of the numerical models in the GNIA and GMNIA as that under concentric solid pressure. The harmonic waves along the meridioanal direction, which have been clear signs of imperfective silo structure under concentric pressure, are not yet observed for the imperfect models (GNIA and GMNIA). The buckling deformations are governed mainly by the distribution of the circumferential and meridional non-uniformity of the solid pressure in a large eccentricity discharge, which is a remarkable distinction from that subject to the concentric solid pressure.

6.3 Critical buckling factor

The load-displacement equilibrium paths in a large eccentricity discharge are also highly nonlinear, and the critical buckling load factors λ_{cr} are listed in Table 6 for various slendernesses of example silos in each buckling analysis. The results are very distinct from those of silos under concentric solid pressure, and reveal that the GMNA or GMNIA, which takes account of the effect of geometrical and material nonlinearity, give out the least value for all example silos from all proposed buckling analysis types. The minor value from critical buckling factor λ_{cr} in the GMNA or GMNIA satisfies the requirement of the overall safety factor 1.65 which is consequently taken as the buckling resistance factor λ_R of the example silos in a large eccentricity discharge.

It is also indicated in Table 6 that the geometrical effect is advantageous for the critical buckling factor λ_{cr} for all slendernesses of example silos. There is an increase in buckling factor by 2.5–3.5 times compared with that under concentric solid pressure. The effect of weld imperfections in a silo under large eccentric discharge shows a distinct variation of critical buckling factor λ_{cr} from that under concentric solid pressure. It is worse for large slenderness of silos and better for small slenderness of silos. For instance, the detrimental effect of weld imperfections decreases the critical buckling factor λ_{cr} by 19% and 21% for the very slender silo (SILO1) and slender silo (SILO2), respectively, while the beneficial effect of weld imperfections increases the critical buckling factor λ_{cr} by 10% and 4% for the squat silo (SILO5) and retaining silo (SILO6), respectively. The complicated effect of weld imperfections on the buckling behavior of silo results from the type of weld depression, the magnitude, the separation and number of imperfections, and most important of all, the asymmetrical distribution of solid pressure during large eccentric discharge. The axisymmetrical weld imperfection type, which has been shown to result in a significant loss of buckling load factor in concentric discharge, seems not to be an appropriate choice for investigation of buckling of silos under large eccentric discharge. In addition, the material nonlinearity is detrimental, and has the most detrimental effect and makes a loss of above 3/4 of the buckling factor λ_{cr}.

6.4 Designed wall thickness and steel consumption index

The designed wall thickness distribution corresponding to the critical buckling factor λ_{cr} in Table 6 and used for buckling analysis is given in Table 7 together with the RCS index. It shows that both the top and bottom thickness of the tapered wall silo under large eccentric discharge are much larger than that under concentric solid pressure, and the bottom thickness in some example silos are even as thick as 88 mm, which is about 1.5 times that of silos under the concentric solid pressure. It indicates, on the one hand, that the non-uniform distribution of solid pressure in a large eccentric discharge has the most detrimental effect on wall thickness and its buckling resistance; on the other, it shows that the effect is over all the height of the silo wall. Designs for silos under large eccentric discharge and concentric discharge are proposed to be carried out independently. The amount of steel used in the example silos ranges from about 204 m^3 to 360 m^3 with the variation of slenderness from retaining to very slender, equivalent to a mass from approximately 1700 t to 2800 t, which is about twice that of silos under concentric discharge. In such cases, the fabrication and flexure of the silo wall become even more complicated during construction. In addition, the thickness in Table 7 is designed to be circumferentially uniform in spite of the non-uniform distribution of solid pressure. This is based on the assumption that the possibility of eccentricity during discharging is identical in every direction, except that the particular operation is arranged to assure a fixed eccentricity direction.

The variation of RCS with the slenderness of example silos under large eccentric discharge is plotted in Fig. 21 together with that under concentric solid pressure for ease of comparison. This shows that the variation of RCS index of the two groups of column is similar and increases rapidly with the

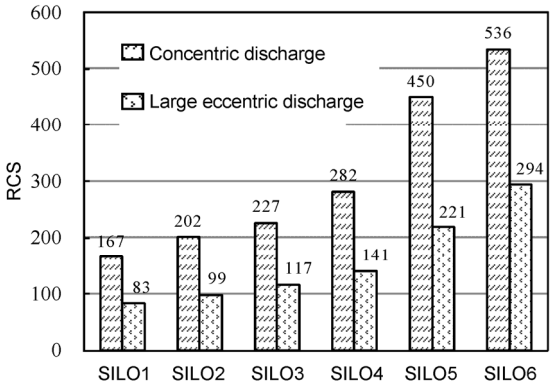

Fig. 21 Relationship of RCS index with slenderness of example silos

Table 6 Critical buckling factors for example silos from proposed buckling analysis types under large eccentricity discharge

No.	Geometry of silo	Critical buckling factor, λ_{cr}					
		LBA	GNA	MNA	GNIA	GMNA	GMNIA
SILO1	Very slender	1.51	5.31	2.73	4.31	2.09	1.66
SILO2	Slender	1.33	4.63	2.49	4.08	1.91	1.68
SILO3	Slender	1.24	4.67	2.54	4.79	1.69	1.74
SILO4	Intermediate slender	1.42	4.61	2.42	5.01	1.71	1.86
SILO5	Squat	1.47	5.64	2.64	6.22	1.68	1.84
SILO6	Retaining	1.16	6.71	1.92	6.96	1.69	1.74

Table 7 Designed wall thickness and economic index of example silos under large eccentricity discharge

No.	Diameter, d_c (m)	Height, h_c (m)	Slenderness, h_c/d_c	t_{top} (mm)	t_{bot} (mm)	t_{eq} (mm)	Capacity (m^3)	Steel consumption (m^3)	RCS
SILO1	20	95.49	4.77	40.0	80.0	60.0	30000	359.99	83.34
SILO2	25	81.49	3.26	40.0	86.0	63.0	40000	403.21	99.20
SILO3	30	70.73	2.36	40.0	88.0	64.0	50000	426.63	117.20
SILO4	35	51.97	1.49	36.0	88.0	62.0	50000	354.29	141.13
SILO5	45	31.44	0.70	32.0	70.0	51.0	50000	226.68	220.57
SILO6	60	21.22	0.35	32.0	70.0	51.0	60000	203.99	294.13

decrease of silo slenderness. Nevertheless, the RCS index of example silos under large eccentric discharge is reduced substantially, at approximately half that of silos under concentric discharge. For instance, the RCS index for the very slender silo (SILO1) is about 167 for concentric discharge, but the value decreases to about 83 for large eccentric discharge. Similarly, the RCS index for the retaining silo (SILO6) is about 536 for concentric discharge, but the value decreases to about 294 for large eccentric discharge. Moreover, for steel silos with a capacity of 50000 m^3, the RCS index for SILO5 is approximately 1.6 times that of SILO4 for concentric discharge. Nevertheless, the value for SILO5 is about 1.57 times that of SILO4 for large eccentric discharge. The squat or retaining silo with small slenderness has the greatest storage efficiency from the economical design viewpoint. The small slendernesses of silos such as squat and retaining silos are strongly proposed in practical structural design for both concentric and large eccentric discharge.

7 Buckling behavior under large eccentricity filling

The diameter of some large steel silos can be as much as 60 m or even larger. They are usually eccentrically filled for technical reasons, such as the limitation of the machinery operation. Even for a concentrically filled silo, the top surface pile during filling or when the silo is full may be formed with a large eccentricity, resulting in asymmetrical solid pressure on the wall and the asymmetrical meridional stresses. The effect of large eccentric filling should be taken into consideration for the intermediate and squat silos when the filling eccentricity is greater than 0.25 times the silo diameter, as is specified by EN 1991-4. Another silo, with a capacity of 50000 m^3 designated as SILO45 in the following analysis, is added to the group of example silos. Its size is: a diameter of 40 m, height of 39.79 m, and slenderness of 0.99. As a result, the buckling behavior of three example silos including SILO4, SILO45, and SILO5 are evaluated for the intermediate and squat silos under large eccentricity filling. This indicates that the magnitude of the asymmetrical friction increases almost linearly with the increase of filling eccentricity, ranging from $0.25d_c$ to $0.50d_c$, with a typical eccentricity of $0.50d_c$ which is deemed as the most detrimental size of eccentricity and adopted in the following numerical evaluation.

7.1 Stress and deformation distribution

In this section, the results of stress and deformation from the LA are presented for the example silos subject to large eccentricity filling pressure, and are shown in Figs. 22 and 23. They indicate that the stress and deformation are highly unevenly distributed in both the circumferential and meridional directions. The maximum meridional stress along the circumference occurs in the zone below the point of the highest wall contact, where the vertical distribution of meridional stress σ_z is plotted in Fig. 22 for example silos. The meridional stress is compressive along the wall height and increases gradually from the top to bottom, while the inflection point is induced at

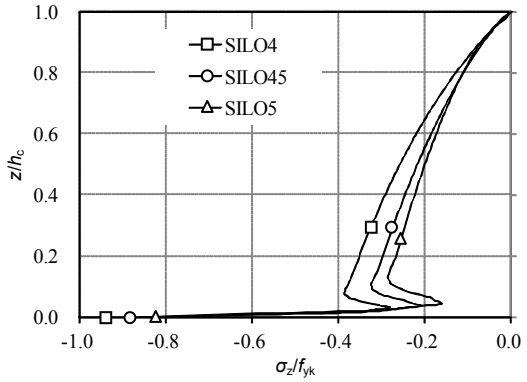

Fig. 22 Distribution of meridional stress of example silos along the wall height

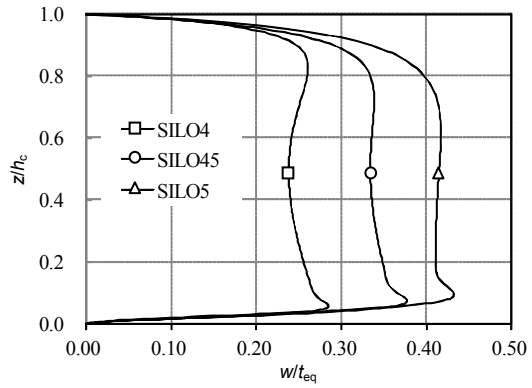

Fig. 23 Distribution of radial displacement of example silos along the wall height

critical height z_{cr} due to the restraint effect of rigid base. The distribution of stress is similar to that of example silos subject to concentric discharge except that the meridional stress is compressive along the whole height of the silo wall. There is no tensile stress induced even if the inflection point and negative moment exist. It is concluded that the meridional stress σ_z is highly unevenly distributed along the height of the silo wall and this is validated to be the main cause of structural buckling of silo.

The radial displacement plotted in Fig. 23 is shown to increase from the top, which reaches its first extremum value w_1 at the critical height z_{cr1} and then decreases slightly until reaches its second extremum value w_2 at the critical height z_{cr2} and vanishes rapidly at the bottom. The maximum radial displacement occurs at the critical height z_{cr2} and is closely dependent on the slenderness of the example silos, and increases significantly with the decrease of silo slenderness.

7.2 Buckling modes

The results show that the buckling deformations from both the linear and nonlinear buckling analyses are asymmetrical, deviating from the center to the side where the most friction locates to the highest wall contact. The linear buckling modes from LBA plotted in Fig. 24 show that the deformations take the form of several meridional waves with assorted magnitudes in the single side. The number of meridional waves is reduced with the decrease of silo slenderness. The nonlinear buckling deformations for geometrically perfect models in the GNA, MNA, and GMNA are similar and occur only at the wall area adjacent to the silo bottom, forming so-called plastic "elephant's failure" modes with consideration of material nonlinearity in the GMNA.

The nonlinear buckling deformations for geometrically imperfect models in the GNIA and GMNIA are also similar and are characterized by a certain number of harmonic waves in the axial direction throughout the whole height of the silo wall, and the number of harmonic waves is almost the same as that of the weld imperfections. Note that the harmonic deformations are also asymmetrical with a much larger amplitude of deformation on the side where most friction locates compared to the other side. In addition, the buckling modes corresponding to the critical buckling point are also plastic combined with the "elephant's failure" deformations at the wall bottom in the GMNIA on account of material plasticity, as is shown in Fig. 25.

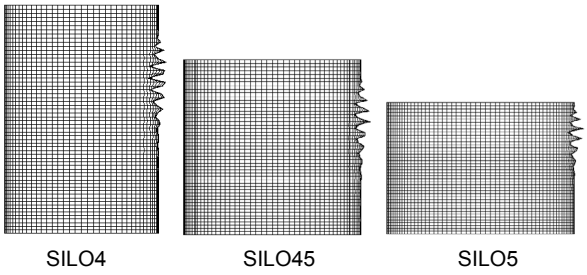

Fig. 24 Buckling modes of the example silos in the LBA

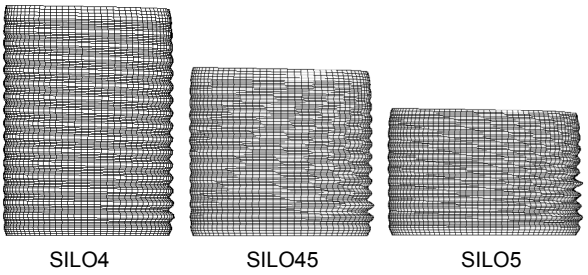

Fig. 25 Buckling modes of the example silos in the GMNIA

7.3 Critical buckling factor

The load-displacement equilibrium paths in large eccentricity filling are also highly nonlinear, and the critical buckling load factors λ_{cr} in each type of buckling analysis are listed in Table 8 for the evaluated example silos. The table shows that the critical load factor from the GMNIA has the least value for all example silos, and the critical buckling factor λ_{cr} in the GMNIA just satisfies the requirement of the overall safety factor 1.65 which is consequently taken as the buckling resistance factor λ_R of the example silos in large eccentricity filling. It is also indicated in Table 8 that the geometrical effect is favorable for the critical buckling factor λ_{cr} for all slendernesses of example silos making about a 5% improvement of the load factor, whereas the material nonlinearity and weld imperfection in the wall are detrimental. The material nonlinearity has the most detrimental effect,

and accounts for a loss of about 30%–50% of the buckling factor λ_{cr}.

7.4 Designed wall thickness and steel consumption index

The designed wall thickness distribution corresponding to the critical buckling factor λ_{cr} in Table 8 and used for buckling analysis is given in Table 9 together with the RCS index. It shows that the designed bottom thickness of the tapered wall silo under large eccentricity filling is about 1.5 times that of silos under the concentric solid pressure, while the designed top thickness remains the same. It indicates that the large eccentric filling pressure has considerable impact on the buckling resistance of the silo, whose effect is mainly centered around the lower part of the wall. The amount of steel used in example silos ranges from about 160 m^3 to 274 m^3 with the variation of slenderness from squat to intermediate slender, equivalent to a mass of between approximately 1200 t and 2200 t, which is about 1.5 times that of silos under concentric discharge. In such cases, the fabrication and flexure of the silo wall also become even more complicated during construction.

The relative relation of economical RCS index is plotted in Fig. 26 for example silos under large eccentric filling together with that under concentric discharge for ease of comparison. It shows that the two groups of RCS index share the similar variable tendency which increases rapidly with the decrease of silo slenderness. Nevertheless, the RCS index of example silos under large eccentric filling is reduced substantially, which is approximately 70% that of silos under concentric discharge.

For instance, the RCS index for the intermediate slender silo (SILO4) is about 282 for concentric discharge, but the value decreases to about 182 for large eccentric filling, a reduction of about 35%. Similarly, the RCS index for the squat silo (SILO5) is about 450 for concentric discharge, but the value decreases to about 312 for large eccentric filling, a reduction of about 30%. Furthermore, for the squat silo (SILO45), the RCS index is 238 which is approximately 1.31 times that of SILO4 and 0.76 times that of SILO5 for large eccentric filling. The conclusion can be drawn that the squat or retaining silos with small slenderness have the best storage efficiency from the economical viewpoint. The small slendernesses of silos such as squat and retaining silos are also preferred in large eccentric filling.

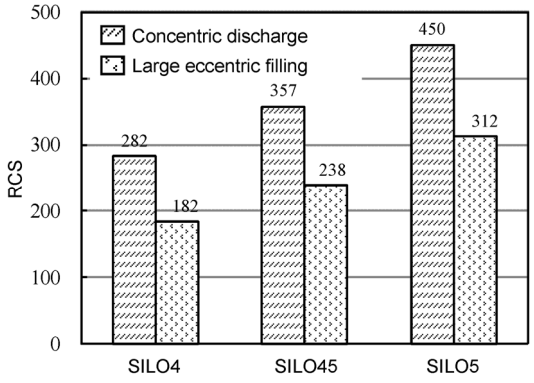

Fig. 26 Relationship of RCS index with slenderness of example silos

Table 8 Critical buckling factors for example silos from proposed buckling analysis types under large eccentricity filling

No.	Geometry of silo	Critical buckling factor, λ_{cr}					
		LBA	GNA	MNA	GNIA	GMNA	GMNIA
SILO4	Intermediate slender	3.81	4.01	3.92	2.84	1.93	1.68
SILO45	Squat	3.45	3.55	3.01	2.94	1.96	1.73
SILO5	Squat	2.87	3.05	2.24	2.44	1.88	1.67

Table 9 Designed wall thickness and economic index of example silos under large eccentricity filling

No.	Diameter, d_c (m)	Height, h_c (m)	Slenderness, h_c/d_c	t_{top} (mm)	t_{bot} (mm)	t_{eq} (mm)	Capacity (m^3)	Steel consumption (m^3)	RCS
SILO4	35	51.97	1.49	6.0	90.0	48.0	50000	274.29	182.29
SILO45	40	39.79	0.99	6.0	78.0	42.0	50000	210.01	238.09
SILO5	45	31.44	0.70	6.0	66.0	36.0	50000	160.02	312.48

8 Conclusions

This paper presented a comprehensive study of the buckling behavior of various slendernesses of large circular steel silos with capacity of 30000–60000 m^3, under the load cases of concentric discharge, large eccentricity discharge, and large eccentricity filling. The studies are demonstrated in accordance with Eurocode, by undertaking six types of buckling analysis on account of the geometrical and material nonlinearity and weld imperfection. The following conclusions can be drawn:

1. The load-displacement curves for nonlinear buckling analysis are highly nonlinear and predict a distinct maximum load followed by a descending path. The silo with smaller slenderness is superior in structural ductility and plasticity to that with a larger slenderness, and the retaining silo or squat silo is preferred in practical structural design.

2. The material nonlinearity is strong and detrimental to buckling behavior of all slendernesses of example silos, resulting in a decrease of buckling resistance for both perfect and imperfect models. The effect of geometrical nonlinearity and weld imperfection on the buckling behavior of steel silos is somewhat complicated, but is closely correlated with silo slenderness, the distribution of solid pressures on silo wall, etc.

3. The economic index called RCS provides an effective measure for the design of steel silos. The results show that the RCS index increases rapidly with the decrease of silo slenderness, where the storage efficiency of a steel silo improved greatly with the slenderness varying from slender silo to retaining silo.

4. The wall thickness type and its distribution have the most important influence on the buckling modes and buckling strength of steel silos. Under the condition of the same amount of steel used in construction, different schemes for wall thickness arrangement are suggested in buckling design of steel silos to achieve the optimal buckling strength.

5. The buckling deformations from both the linear and nonlinear buckling analyses in large eccentric discharge are strongly asymmetrical arising from the circumferential and meridional non-uniform distribution of the solid pressures. The buckling is mainly governed by the non-uniform distribution of the solid pressures other than other influential factors such as weld imperfection and geometrical and material nonlinearity, compared with the load case of concentric pressure. The linear and nonlinear buckling deformations in large eccentric filling are also asymmetrical, deviating from the center to the side where the most friction locates to the highest wall contact.

6. Large eccentricity both in discharge and filling would result in a strong decrease of storage efficiency of a steel silo. The RCS index of example silos under large eccentricity discharge and filling is reduced substantially, and is approximately half and 70% that of silos under concentric discharge, respectively.

References

ANSYS, 2008. ANSYS User's Manual. Swanson Analysis Systems Inc., Houston, USA.

BSI (British Standards Institution), 2002a. Basis of Structural Design, BS EN 1990:2002. BSI, UK.

BSI (British Standards Institution), 2002b. Actions on Structures-Part 1-1: General Actions–Densities, Self-weight, Imposed Loads for Buildings, BS EN 1991-1-1:2002. BSI, UK.

BSI (British Standards Institution), 2005. Design of Steel Structures-Part 1-1: General Rules and Rules for Buildings, BS EN 1993-1-1:2005. BSI, UK.

BSI (British Standards Institution), 2006. Actions on Structures-Part 4: Silos and Tanks, BS EN 1991-4:2006. BSI, UK.

BSI (British Standards Institution), 2007a. Design of Steel Structures-Part 1-6: Strength and Stability of Shell Structures, BS EN 1993-1-6:2007. BSI, UK.

BSI (British Standards Institution), 2007b. Design of Steel Structures-Part 4-1: Silos, BS EN 1993-4-1:2007. BSI, UK.

Gillie, M., Rotter, J.M., 2002. The effects of patch loads on thin-walled steel silos. *Thin-Walled Structures*, **40**(10): 835-852. http://dx.doi.org/10.1016/S0263-8231(02)00028-9

Gillie, M., Holst, J.M.F.G., 2003. Structural behaviour of silos supported on discrete, eccentric brackets. *Journal of Constructional Steel Research*, **59**(7):887-910. http://dx.doi.org/10.1016/S0143-974X(02)00078-0

Greiner, R., Guggenberger, W., 1998. Buckling behaviour of axially loaded steel cylinders on local supports-with and without internal pressure. *Thin-Walled Structures*, **31**(1-3): 159-167. http://dx.doi.org/10.1016/S0263-8231(98)00011-1

ISO (International Organization for Standardization), 1995. Basis for Design of Structures-Loads Due to Bulk Materials, ISO 11697:1995. ISO.

Iwicki, P., Tejchman, J., Chroscielewski, J., 2014. Dynamic FE simulations of buckling process in thin-walled cylindrical metal silos. *Thin-Walled Structures*, **84**:344-359. http://dx.doi.org/10.1016/j.tws.2014.07.011

Kim, S.E., Kim, C.S., 2002. Buckling strength of the

cylindrical shell and tank subjected to axially compressive loads. *Thin-Walled Structures*, **40**(4):329-353. http://dx.doi.org/10.1016/S0263-8231(01)00066-0

Li, B.R., Wang, X.Y., Ge, H.L., *et al.*, 2005. Study on applicability of modal analysis of thin finite length cylindrical shells using wave propagation approach. *Journal of Zhejiang University-SCIENCE A*, **6**(10):1122-1127. http://dx.doi.org/10.1631/jzus.2005.A1122

Pircher, M., Bridge, R.Q., 2001. Buckling and post-buckling behaviour of silos and tanks under axial load-some new aspects. *Journal of Structural Engineering*, **127**(10):1129-1136. http://dx.doi.org/10.1061/(ASCE)0733-9445(2001)127:10(1129)

Rotter, J.M., Teng, J.G., 1989. Elastic stability of cylindrical shells with weld depressions. *Journal of Structural Engineering*, **115**(5):1244-1263. http://dx.doi.org/10.1061/(ASCE)0733-9445(1989)115:5(1244)

Rotter, J.M., Zhang, Q., 1990. Elastic buckling of imperfect cylinders containing granular solids. *Journal of Structural Engineering*, **116**(8):2253-2271. http://dx.doi.org/10.1061/(ASCE)0733-9445(1990)116:8(2253)

Sadowski, A.J., Rotter, J.M., 2011a. Buckling of very slender metal silos under eccentric discharge. *Engineering Structures*, **33**(3):1187-1194. http://dx.doi.org/10.1016/j.engstruct.2010.12.040

Sadowski, A.J., Rotter, J.M., 2011b. Steel silos with different aspect ratios-I: behaviour under concentric discharge. *Journal of Constructional Steel Research*, **67**(10):1537-1544. http://dx.doi.org/10.1016/j.jcsr.2011.03.028

Sadowski, A.J., Rotter, J.M., 2011c. Steel silos with different aspect ratios-II: behaviour under eccentric discharge. *Journal of Constructional Steel Research*, **67**(10):1545-1553. http://dx.doi.org/10.1016/j.jcsr.2011.03.027

Sadowski, A.J., Rotter, J.M., 2012. Structural behavior of thin-walled metal silos subject to different flow channel sizes under eccentric discharge pressures. *Journal of Structural Engineering*, **138**(7):922-931. http://dx.doi.org/10.1061/(asce)ST.1943-541X.0000530

Sadowski, A.J., Rotter, J.M., 2013. Buckling in eccentrically discharged silos and the assumed pressure distribution. *Journal of Engineering Mechanics*, **139**(7):858-867. http://dx.doi.org/10.1061/(asce)EM.1943-7889.0000525

Song, C.Y., 2002. Buckling of un-stiffened cylindrical shell under non-uniform axial compressive stress. *Journal of Zhejiang University-SCIENCE*, **3**(5):520-531. http://dx.doi.org/10.1631/jzus.2002.0520

Song, C.Y., 2004. Effects of patch loads on structural behavior of circular flat-bottomed steel silos. *Thin-Walled Structures*, **42**(11):1519-1542. http://dx.doi.org/10.1016/j.tws.2004.05.009

Song, C.Y., Teng, J.G., 2003. Buckling of circular steel silos subject to code-specified eccentric discharge pressures. *Engineering Structures*, **25**(11):1397-1417. http://dx.doi.org/10.1016/S0141-0296(03)00105-6

Standards Australia, 1996. Loads on Bulk Solids Containers, AS 3774-1996. Standards Australia, Sydney, Australia.

Zhao, Y., Cao, Q.S., Xie, X.Y., 2006. Floating-roof steel tanks under harmonic settlement: FE parametric study and design criterion. *Journal of Zhejiang University-SCIENCE A*, **7**(3):398-406. http://dx.doi.org/10.1631/jzus.2006.A0398

中文概要

题　目： 多种长细比的大型钢筒仓结构的屈曲设计

目　的： 大型钢筒仓结构在正常装卸料过程中极易发生各种失稳破坏。本文旨在分析多种长细比的大型钢筒仓结构在散料荷载作用下的屈曲性能，为结构的稳定设计提供理论依据及技术支持。

创新点： 1. 提出散料荷载作用下大型钢筒仓结构屈曲分析的 4 种典型工况：轴对称卸料荷载工况、小偏心卸料荷载工况、大偏心卸料荷载工况和大偏心装料荷载工况；2. 建立了适用于不同屈曲分析类型的多种数值模型，研究了结构的稳定性能，并分析了各种非线性、初始几何缺陷、仓壁厚度的分布和基底嵌固刚度等对结构稳定性能的影响。

方　法： 1. 根据不同工况下散料荷载分布的特点和屈曲分析类型的差异，通过非线性有限元方法，研究结构在四种散料荷载工况下的稳定性能；2. 通过研究结构在各种非线性屈曲分析下的荷载-位移全过程响应，确定结构的屈曲临界荷载和结构的稳定承载力；3. 比较各种荷载工况下结构的屈曲临界荷载、屈曲模态及仓壁厚度分布特点，分析结构用钢量指标的变化。

结　论： 1. 非线性屈曲分析的荷载-位移曲线是高度非线性的，不同长细比钢筒仓的屈曲平衡路径之间有较大差异。2. 钢筒仓结构的屈曲延性随长细比的减小而显著增大。3. 材料非线性对结构的稳定性极为不利；几何非线性和初始几何缺陷对结构稳定性能的影响与结构的长细比密切相关。4. 壁厚的分布对钢筒仓的稳定承载力和屈曲模态影响很大；设计时应考虑仓壁壁厚的不同组合形式，并确定使结构取得最大稳定承载力的仓壁最优分布形式。5. 装料或卸料过程中的偏心使结构的储存效率（容耗比指标）显著降低。

关键词： 钢筒仓；壳体；偏心卸料；屈曲稳定；非线性